Article | Open Access

Energy Materials

Long *et al. Energy Mater.* **2026**, *6*, 600069 **DOI:**10.20517/energymater.2026.52

All-solid-state proton batteries with a wide operation-temperature range of 160 °C

Lifen Long[1], Yike Huang[1], Yun Zheng[1], Yan Guo[1], Yinan Liu[1], Yingying Shen[1], Pingshan Jia[1], Zikang Xu[1], Shengyang Dong[1,2,*], Huaiyu Shao[1,*]

Keywords:
Proton batteries, solid-state electrolyte, zirconium hydrogen phosphate, wide temperature range, high stability

Citation: Long, L.; Huang, Y.; Zheng, Y.; Guo, Y.; Liu, Y.; Shen, Y.; Jia, P.; Xu, Z.; Dong, S.; Shao, H. All-solid-state proton batteries with a wide operation-temperature range of 160 °C. *Energy Mater.* **2026**, *6*, 600069. https://dx.doi.org/10.20517/energymater.2026.52

Received: 2 Apr 2026
First Decision: 30 Apr 2026
Revised: 2 Jun 2026
Accepted: 12 Jun 2026
Published: 29 Jun 2026

Academic Editor:
Sining Yun
Copy Editor:
Xing-Yue Zhang
Production Editor:
Xing-Yue Zhang

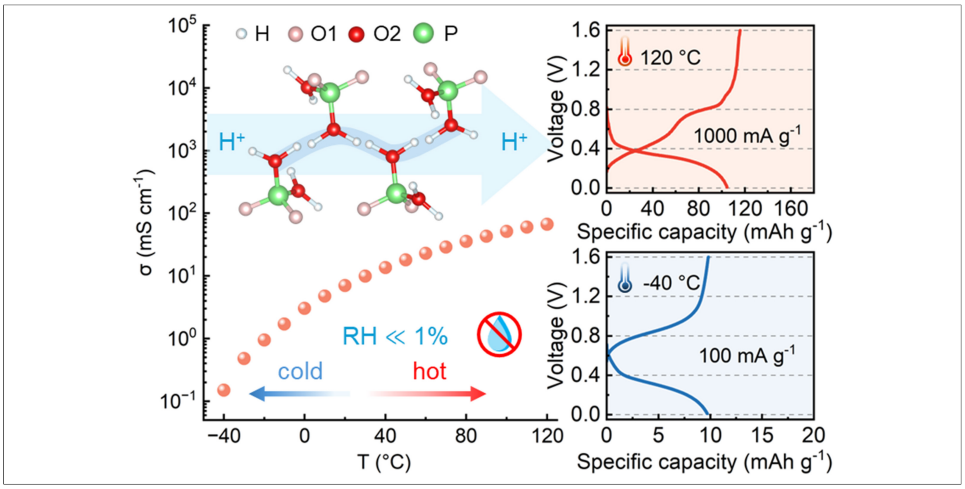

Abstract

All-solid-state proton batteries are promising energy storage systems, in which the solid-state proton electrolyte plays an important role. However, achieving fast proton conduction over a wide temperature range is challenging. Here, we report zirconium hydrogen phosphate (ZHP) as a solid-state proton electrolyte. It shows ultra-high proton conductivity from -40 to 120 °C (0.15 to 66.76 mS·cm^{-1}), a wide stability window (~5.5 V), and excellent long-term stability. Batteries using ZHP as electrolyte exhibit stable operation over a wide temperature range (160 °C), and retain 92% capacity after 12,000 cycles at room temperature. After 1,000 cycles, the batteries retain 100% capacity at -30 °C and 84.5% at 40 °C. This work provides new insights into the design and application of all-solid-state proton batteries capable of operating over a wide temperature range.

[1]Institute of Applied Physics and Materials Engineering, University of Macau, Macau 999078, China.
[2]Jiangsu Key Laboratory of New Energy Devices & Interface Science, School of Chemistry and Materials Science, Nanjing University of Information Science and Technology, Nanjing 210044, Jiangsu, China.

[*]**Correspondence to:** Prof. Huaiyu Shao, Institute of Applied Physics and Materials Engineering, University of Macau, Macau 999078, China. E-mail: hshao@um.edu.mo; Prof. Shengyang Dong, Jiangsu Key Laboratory of New Energy Devices & Interface Science, School of Chemistry and Materials Science, Nanjing University of Information Science and Technology, Nanjing 210044, Jiangsu, China. E-mail: dongsyst@nuist.edu.cn

INTRODUCTION

Proton batteries are considered promising next-generation energy storage technologies. Proton carriers possess a small ionic radius, low mass, and fast kinetics. In addition, proton-based systems benefit from abundant resources and environmental friendliness[1-6]. At present, aqueous electrolytes are widely used in proton batteries owing to their ultra-high proton conductivity, which enables fast proton transport and favorable electrochemical kinetics[4,7-10]. However, acid aqueous electrolytes can corrode current collector and dissolve electrode materials, leading to active material loss and capacity fading. Additionally, the narrow redox window of water (1.23 V) promotes hydrogen and oxygen evolution during operation, limiting the working voltage and causes severe gas evolution[11]. To address these issues, researchers have proposed "water-in-salt" and "water-in-sugar" electrolytes. Although they broaden the electrochemical stability window, water-related side reactions remain unavoidable[12-14]. Non-aqueous electrolytes including anhydrous phosphoric acid (H_3PO_4 in acetonitrile, H_3PO_4/MeCN)[15], organic gel polymers[16], protonated organic ionic liquids, and ionic liquid organic solvent solutions, have also been explored[17-19]. However, the inorganic-organic systems may suffer from phase separation. Organic polymer gels often depend on humidity, and organic solvents can be volatile and flammable[20]. Therefore, developing electrolytes that provide high proton conductivity, a wide electrochemical stability window, stable conductivity over a wide temperature range and long-term durability at the same time remains a key challenge for proton batteries.

Solid-state electrolytes offer a promising route to overcoming the limitations of liquid proton electrolytes. They can broaden the electrochemical window, increase the operating voltage, suppress gas evolution issues, and mitigate the corrosion of electrodes and current collectors, thereby improving the long-term cycling stability of proton batteries. Currently, several types of solid-state proton electrolytes have been developed, including perfluorosulfonic acid polymer electrolytes, polybenzimidazole (PBI), layered hydrates, heteropoly acids (HPAs), metal-organic frameworks (MOFs), covalent organic frameworks (COFs), and solid acids with tetrahedral oxyanion groups (such as CsH_2PO_4)[21-32]. Most organic solid-state electrolytes rely on guest molecules or functional groups for proton conduction. As a result, their conductivity is highly sensitive to ambient temperature and humidity during application. For example, the conductivity of perfluorosulfonic acid polymer electrolytes drops sharply with decreasing humidity, while batteries using glassy polymer electrolytes require around 110 °C for stable operation. Many inorganic solid-state electrolytes also suffer from limited operating conditions. For example, CsH_2PO_4, achieves high conductivity only at elevated temperature restricting its operating conditions. To overcome these limitations, several solid-state and quasi-solid-state electrolytes have been reported, such as zirconium acid triphosphate (ZP3), MOF-based and COF-based solid proton electrolytes, acid-in-clay electrolytes (AiCEs), and dual-acid quasi-solid-state electrolyte (SSAE)[32-37]. Although these strategies alleviate the dependence on strict humidity and temperature control, several issues remain. ZP3 has mainly been studied for its ion conduction characteristics, especially at high temperatures. AiCEs can only work at low and room temperatures. In addition, MSA@ZIF-8-C-X and MeSA@PBI-COF electrolytes show limited rate performance and long-term cycling stability, there are low temperature performance remains unclear. Overall, the electrochemical performance of solid-state proton electrolytes over a wide temperature range has received limited attention. Therefore, developing new anhydrous solid-state proton electrolytes with high conductivity over a wide temperature range (high, room, and low temperatures) remains a great challenge in proton batteries.

Here, we report zirconium hydrogen phosphate (ZHP) as a wide temperature solid-state electrolyte and fabricate an all-solid-state proton battery based on this material. ZHP helps address key challenges in proton batteries, including gas evolution, electrolyte corrosion, and limited operation at low and high temperatures. Compared with previously reported liquid and solid-state electrolytes, ZHP exhibits outstanding proton conductivity over a wide temperature range from -40 to 120 °C, reaching 0.15 to 66.76 $mS \cdot cm^{-1}$. It also delivers a wide electrochemical stability window, good thermal stability, and excellent compatibility with

both electrodes and current collectors. To assemble the solid-state proton battery, Prussian blue analogue (PBA)-type cathodes and MoO_3 anodes are widely investigated for proton batteries. PBA-type cathodes provide open frameworks and tunable redox centers for reversible proton storage, while MoO_3 anodes enable reversible proton insertion/extraction though Mo redox reactions[38-40]. Benefiting from the superior properties of ZHP electrolyte, the resulting all-solid-state proton battery operates stably over a 160 °C temperature range, from -40 to 120 °C. The batteries deliver remarkable cycling durability, with only 8% capacity decay after 12,000 cycles at room temperature, negligible degradation after 1,000 cycles at -30 °C, and 84.5% capacity retention after 1,000 cycles at 40 °C.

EXPERIMENTAL

Materials

Acetone (AR) was purchased from Sinopharm Chemical Reagent Co., Ltd. Phosphoric acid (H_3PO_4, 99%, Crystalline), copper sulfate analytical titrant ($CuSO_4$, 0.5 M), potassium ferricyanide [$K_3Fe(CN)_6$, 99%], molybdenum trioxide (MoO_3, 99.9% metals basis), hydrazine hydrate (35 wt.% in water), N-methyl-2-pyrrolidone (NMP, 99.5%), poly(vinylidene fluoride) (PVDF) and zirconium (IV) oxychloride octahydrate ($ZrOCl_2 \cdot 8H_2O$, 99.9%) were purchased from Shanghai Macklin Biochemical Technology Co., Ltd. Conductive carbon (Super P) was purchased from Guangdong Canrd New Energy Technology Co., Ltd. All these chemicals were used as received without further purification.

Preparation of ZHP and H-TBA

ZHP was prepared by heating and stirring, with minor modifications based on the previous report[32]. Briefly, $ZrOCl_2 \cdot 8H_2O$ was first dried at 250 °C. ZHP was synthesized by reacting $ZrOCl_2$ (0.785 g) with molten H_3PO_4 (15 g) at 85 °C under stirring for 72 h. The precipitate was collected by centrifugation, washed with acetone, and dried at 80 °C. Pre-protonated Turnbull's blue analogue (H-TBA) was obtained via a controlled coprecipitation process[9,41]. A $CuSO_4$ solution (40 mL, 0.2 M) was added dropwise into the $K_3Fe(CN)_6$ solution (40 mL, 0.1 M) under continuous stirring. The mixture was stirred for 6 h, yielding an olive-green precipitate. The precipitate (1 g) was redispersed in 100 mL of deionized water, followed by the addition of hydrazine solution (50 mL, 0.05 M) and further stirring for 2 h. After the reaction, the solid was collected by centrifugation, washed repeatedly, and dried at 40 °C for 12 h.

Preparation of electrolytes and electrodes

ZHP electrolyte pellets were obtained with ~1 mm thickness by pressing 200 mg of ZHP powder in a metal die with a diameter of ~10 mm. The powder was pressed at ~400 MPa using an automatic powder press. Cathode slurries were prepared by mixing the active materials, Super P and PVDF in a weight ratio of 7:2:1, with NMP added as solvent. The mixtures were mixed mechanically until a uniform slurry was obtained. Then the slurry was coated on commercial titanium (Ti) foils or aluminum (Al) foils and dried at 60 °C for 12 h. For the MoO_3 anodes, the commercial MoO_3 powder was used as the active material directly, and the preparation method is the same as above.

Electrochemical characterizations

All-solid-state batteries were assembled in a glove box filled with argon gas, and their electrochemical performance was evaluated in CR2032-type coin cells with the Neware CT-4008 system. In addition, no liquid electrolyte or wetting liquid was added during the assembly of the all-solid-state proton battery with ZHP. Full cells of H-TBA/ZHP/MoO_3 were assembled to evaluate long-term stability at various temperatures in a variable temperature oven, and rate performance at room temperature. Galvanostatic charge/discharge (GCD) curves at various temperatures were recorded after equilibrating the battery at each temperature for 30 min. Ti/ZHP/Pt cells, Pt as reference/counter electrodes and Ti foils as working electrodes, were utilized to measure the linear sweep voltammetry (LSV) between -3 and 4 V (*vs.* Pt^{2+}/Pt) at 5 $mV \cdot s^{-1}$ on a CHI 760e

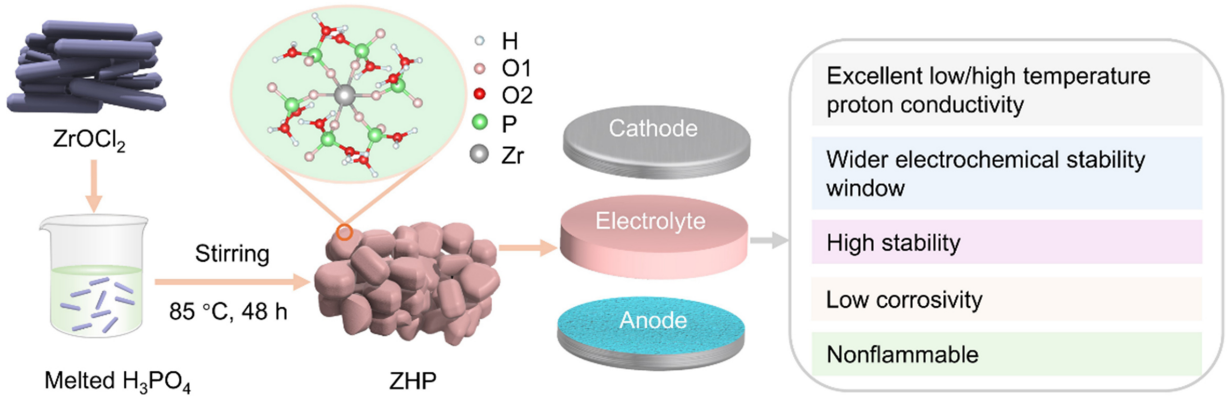

Figure 1. Schematic illustration of the preparation of ZHP and its advantages as a solid-state proton electrolyte. ZHP was synthesized from $ZrOCl_2$ and molten H_3PO_4, and then used as electrolyte in all-solid-state proton batteries. ZHP: Zirconium hydrogen phosphate.

electrochemical workstation. When conducting the LSV test on aqueous-based coin cells, the electrolyte was a 1 M phosphoric acid solution, filter paper was used as the separator, and electrodes were the same as those used in the solid-state coin cells test. Electrochemical impedance spectroscopy (EIS) was measured using stainless steel symmetric cells with ZHP on Solartron 1260A frequency response analyzer.

Material characterization

The crystal structure was analyzed by powder X-ray diffraction (XRD, Rigaku SmartLab, Cu Kα1), and the obtained data were refined by the Rietveld method using the GSAS II software package[42]. Morphology and particle size were characterised by transmission electron microscopy (TEM, Talos F200S, 200 kV) and scanning electron microscopy (SEM, Zeiss Sigma). Elemental distribution was analyzed by energy-dispersive X-ray spectroscopy (EDS). *In situ* optical observations were conducted using an optical microscope (Olympus SZX16) equipped with a custom *in situ* setup. The ^{1}H solid-state nuclear magnetic resonance (SSNMR) spectra were recorded on a Bruker AVANCE NEO 400WB spectrometer. Structural features were further obtained from Fourier transform infrared spectroscopy (FTIR, SHIMADZU IRSpirit-TX). Thermal stability was evaluated by thermogravimetric analysis (TGA, SDT Q600 V20.9 Build 20) at a heating rate of 5 °C·min^{-1} in a N_2 atmosphere. The elemental composition was measured by inductively coupled plasma optical emission spectroscopy (ICP-OES, Agilent 720ES).

Computational simulation analysis

Bond-valence site energy (BVSE) calculation was used in the softBV program[43-45] using the Rietveld-refined structural model as input. The proton (H^+) energy landscape was constructed on a grid with a resolution of 0.05 Å. The diffusion paths were identified by visualizing the isosurfaces and calculating the energy region of the low bond-valence site energy of the pathway. The migration energy barrier was estimated from the BVSE energy profile along the diffusion pathway.

RESULTS AND DISCUSSION

Zirconium hydrogen phosphates represent a group of inorganic solid-state acids that can form different crystal structures depending on the P/Zr molar ratio and synthesis conditions[32,46]. ZHP was synthesized from $ZrOCl_2$ and H_3PO_4 via precipitation [Figure 1 and Supplementary Figure 1]. To determine the chemical formula of the obtained ZHP, ICP-OES, TGA, and XRD were used. ICP-OES results [Supplementary Table 1] revealed a Zr:P molar ratio of 1:3.2. The TGA curve [Figure 2A] shows two distinct mass loss stages. The first stage, occurring from 160 to 450 °C, corresponds to the removal of water molecules associated with the condensation of P-OH groups in ZHP. The second stage, from 450 to 1,200 °C, is attributed to the

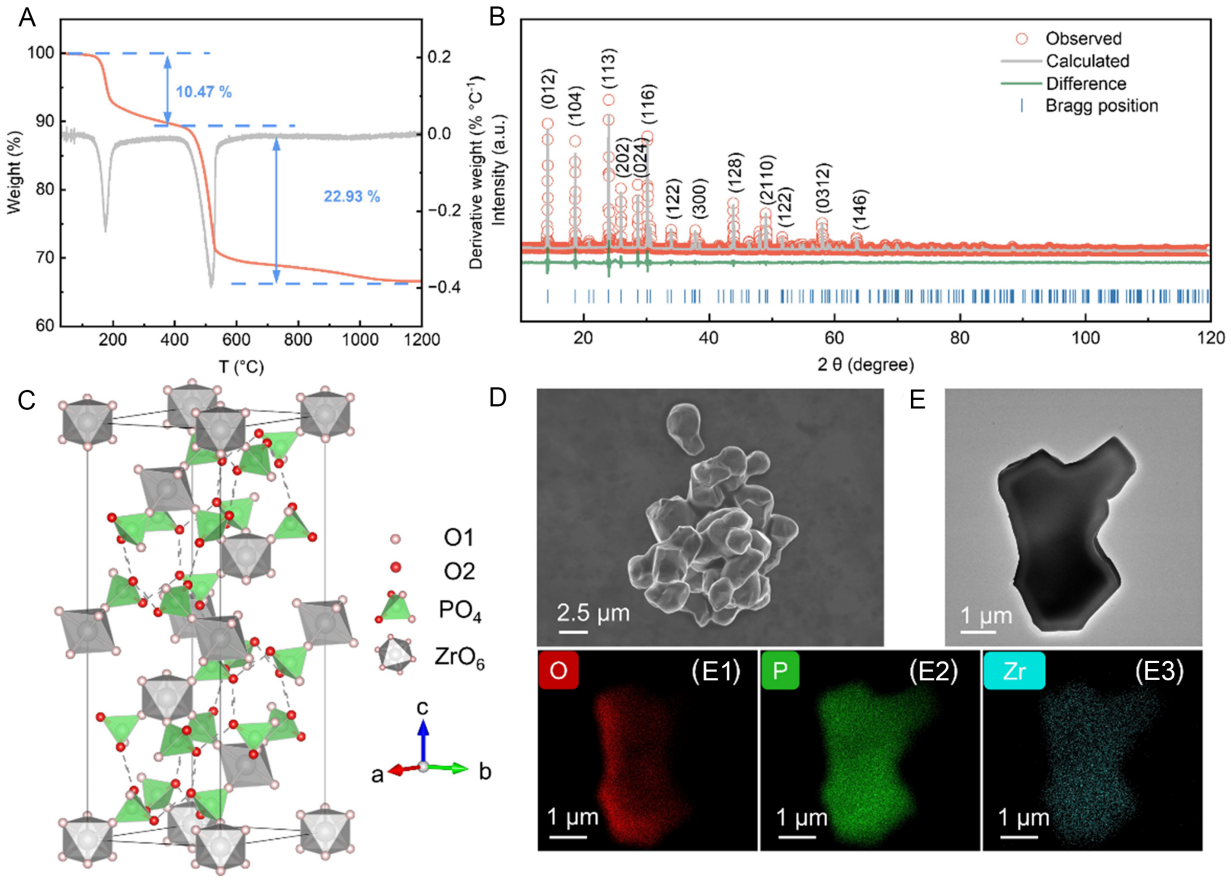

Figure 2. Physical characterization of ZHP. (A) TGA curves; (B) Rietveld refinement of the XRD pattern; (C) Layered crystal structure (ZrO_6/PO_4); (D) SEM image of ZHP; (E) TEM image with O, P, and Zr elemental mappings (E1-E3). ZHP: Zirconium hydrogen phosphate; TGA: thermogravimetric analysis; XRD: X-ray diffraction; SEM: scanning electron microscopy; TEM: transmission electron microscopy.

sublimation of P_2O_5 and further dehydration[47]. Consistent with the XRD pattern of the final residue [Supplementary Figure 2], the remaining solid after TGA is identified as ZrP_2O_7. The total mass loss across both stages is 33.4%. Based on the above results, the chemical formula of the synthesized ZHP is determined to be $ZrH_{5.4}P_{3.2}O_{12.7}$.

The crystal structure of ZHP was determined by Rietveld structure refinement of the XRD data collected at room temperature. The results are shown in Figure 2B and Supplementary Table 2, with the reliability factors of Rp = 6.17% and Rwp = 4.37%. ZHP is a trigonal structure (space group of R-3c) with a lattice constant of a = 8.25738 Å, b = 8.25738 Å, c = 25.6243 Å, vol = 1,513.099 Å^3. The atomic bond lengths and angles are listed in Supplementary Table 3. The crystal structure schematic of the ZHP unit cell is shown in Figure 2C. The structure is layered and consists of ZrO_6 octahedra and PO_4 tetrahedra connected by corner sharing. Each Zr atom is coordinated to six oxygen atoms (O1), each O1 shared with one phosphate unit. In addition, each P atom is also bonded to another oxygen atom in a different chemical environment from O1. This oxygen is denoted as O2 and plays a crucial role in the formation of the internal hydrogen bonds in ZHP.

The morphology of ZHP was observed by SEM. The SEM image shows that ZHP consists of many irregular particles, as depicted in Figure 2D. TEM and its corresponding elemental mapping were used to further characterise ZHP. The results show that Zr, P and O elements are uniformly distributed in ZHP particles [Figure 2E, E1-E3].

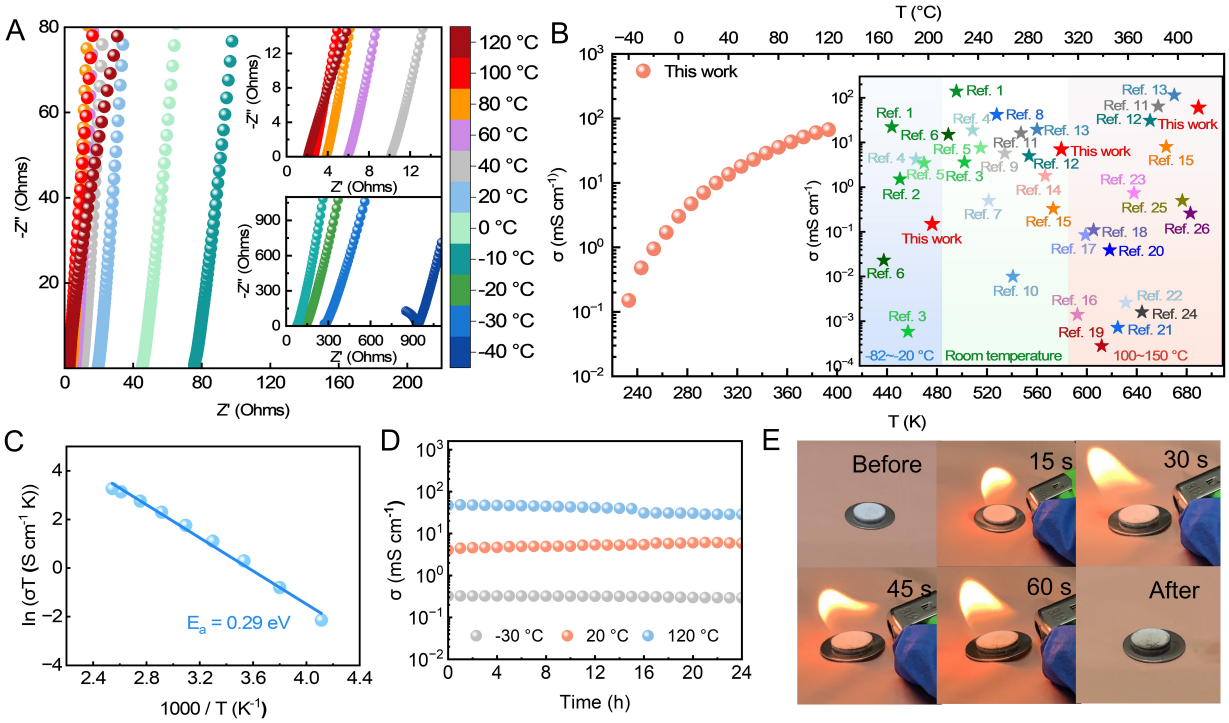

Figure 3. Characterization of ZHP electrolyte. (A) Nyquist plots of ZHP at various temperatures under dry conditions (RH≪1%); (B) Temperature-dependent proton conductivity of ZHP. The inset diagram is ionic conductivity of ZHP compared with other electrolytes at the same temperature; (C) Arrhenius fitting curves for the proton conductivity of ZHP; (D) The proton conductivity of ZHP has long-term stability at various temperatures; (E) Flame test of ZHP. ZHP: Zirconium hydrogen phosphate; RH: relative humidity.

Alternating-current (AC) impedance analyses were conducted to evaluate the proton conductivity of the synthesized ZHP. Dense ZHP pellets (~1 mm thick and 10 mm in diameter; Supplementary Figure 3) were used for conductivity measurement. Each pellet was sandwiched between two stainless-steel sheets, sealed in coin cells and tested under anhydrous conditions [Supplementary Figure 4] from -40 to 120 °C. The Nyquist plots of ZHP at various temperatures are presented in Figure 3A. With increasing temperature, the impedance response gradually becomes more linear. The combination of semicircular and linear regions is observed at -40 and -30 °C, suggesting combined contributions from bulk resistance and electrode-electrolyte interfacial effects. This behavior is commonly observed in highly conductive proton electrolytes with high characteristic frequencies[31,33,48]. Since the impedance spectra at other temperatures mainly show nearly linear responses, the bulk resistance was determined from the high-frequency intercept on the Z′ axis for consistent comparison over the whole temperature range. The corresponding temperature-dependent proton conductivity is shown in Figure 3B, exhibiting a clear increase with temperature. Notably, ZHP delivers high proton conductivity across the investigated range. ZHP shows significantly fast proton conduction, reaching 0.15 mS·cm^{-1} at -40 °C, 7.04 mS·cm^{-1} at 20 °C and 66.76 mS·cm^{-1} at 120 °C. As shown in Supplementary Figure 5, no obvious linear relationship is observed between the thickness of the ZHP electrolyte and its ionic conductivity. This indicates that the measured conductivity reflects the intrinsic proton-transport properties of the material. Interestingly, as shown in the inset of Figure 3B and Supplementary Table 4, the conductivity of ZHP from -40 °C to room temperature is comparable to that of some solid-state proton electrolytes measured under high humidity conditions, such as $H_5SiMo_{11}VO_{40}·8H_2O$[25]. From room temperature to 120 °C, the proton conductivity of ZHP is higher than that of solid-state proton electrolytes capable of operating at high temperatures, such as crystalline metal-organic framework[49], ionic plastic crystal[50], proton-conductive coordination polymer glass $\{[Zn_3(H_2PO_4)_6(H_2O)_3](BTA)\}$[48], $(CsH_2PO_4)_{0.85}(H_3PO_4)_{0.15}$[51], and ZP3[32]. In addition, *in situ* variable temperature XRD confirms the remarkable thermal stability of ZHP, with no obvious phase transitions or

structural degradation from -40 to 120 °C [Supplementary Figure 6]. This result suggests that the proton-transport framework in ZHP maintains its stability over a wide temperature range, and that the structure does not undergo a temperature-induced phase transition. This behavior differs from that of some solid-state proton electrolytes such as {[$Zn_3(H_2PO_4)_6(H_2O)_3$](BTA)}[48], which experiences a significant decrease in proton conductivity at room temperature. Moreover, ZHP offers distinct advantages compared to the previously reported solid-state proton conductors that operate only from low to room temperatures or from room temperature to high temperatures. Consequently, these results indicate that ZHP is a promising solid-state proton electrolyte for extensive application in electrochemical devices.

The activation energy (E_a) for proton transfer was obtained from Arrhenius fitting of the conductivity data. As shown in Figure 3C, ZHP exhibits a small E_a value of 0.29 eV (< 0.4 eV), suggesting that proton migration is primarily dominated by the Grotthuss mechanism[52]. Moreover, the E_a value is close to the activation energy (0.278 eV) obtained through simulation calculation, as shown in Supplementary Figure 7. In addition, abundant P-OH groups in ZHP form the O···OH networks [Supplementary Figures 8 and 9]. A one-dimensional conduction pathway also exists within the hydrogen-bond networks of ZHP, which is beneficial for enhancing the ability of rapid proton transfer [Supplementary Figure 10]. These hydrogen-bond networks are similar to those formed by H_3PO_4 and are frustrated due to the imbalance in the number of proton acceptors and donors. Such a frustrated hydrogen-bond network can facilitate rapid proton movement related to long distances[32,53,54]. Therefore, these results indicate that the superior proton conductivity of ZHP is mainly attributed to its intrinsic and stable P-OH-based hydrogen-bond network within the robust Zr-O-P framework. The stable inorganic framework helps preserve the proton-conduction pathways over a wide temperature range, while the abundant P-OH groups and frustrated hydrogen-bond network enable continuous proton transfer. Many phosphate-based solid-state proton electrolytes, such as hydrated zirconium phosphates and alkali-metal dihydrogen phosphates, show proton transport affected by hydration state, dehydration, or phase transitions[55-57]. In contrast, ZHP maintains more stable proton conduction under anhydrous and wide-temperature conditions. Furthermore, the long-term stability of proton conduction was studied by monitoring time-dependent proton conductivity at -30, 20 and 120 °C, as shown in Figure 3D. The results demonstrate proton conduction of ZHP without significant reduction at these temperatures after 24 h of operation. LSV measurements [Supplementary Figure 11] were conducted to evaluate the electrochemical stability window of ZHP. ZHP shows a wider electrochemical stability window of ~5.5 V (-2.5 to 3 V *vs.* Pt^{2+}/Pt), compared with ~2.2 V (-1.4 to 0.8 V *vs.* Pt^{2+}/Pt) for the 1 M H_3PO_4 aqueous solution. This can be ascribed to the absence of free water molecules in ZHP compared with the H_3PO_4 aqueous solution. This enhanced stability contributes to long-term cycling performance and relaxes the requirements for electrode materials. In addition, the nonflammability and high safety of the ZHP were verified by flame test, as shown in Figure 3E. ZHP demonstrated almost no flammability while being kept in direct contact with the flame for 1 min.

Given its remarkable proton conductivity, ZHP shows strong promise as a solid-state proton electrolyte for proton batteries. However, solid-state proton batteries remain relatively underdeveloped because of the lack of solid-state electrolytes capable of delivering sufficient proton conduction under anhydrous conditions. To date, several examples of solid-state proton electrolytes used in proton batteries have been reported, including the AiCEs[36], [$Zn_3(H_2PO_4)_6(H_2O)_3$](BTA)[48], MSA@ZIF-8-C-X[33], and MeSA@PBI-COF[34]. To demonstrate the feasibility of ZHP as a solid-state electrolyte for proton batteries, a cathode (H-TBA), commercial MoO_3 anodes, and Ti foil current collectors were used to assemble all-solid-state proton batteries. The cell schematic is shown in Figure 4A, and the physical characterization of the cathode and anode is shown in Supplementary Figures 12-14. Figure 4B and C show the rate performance and the corresponding GCD profiles of the H-TBA/ZHP/MoO_3 cell. At room temperature, the cell delivers specific capacities of 44 mAh·g^{-1} at 10 mA·g^{-1} and maintains 8 mAh·g^{-1} even at a high current density of 3,000 mA·g^{-1}.

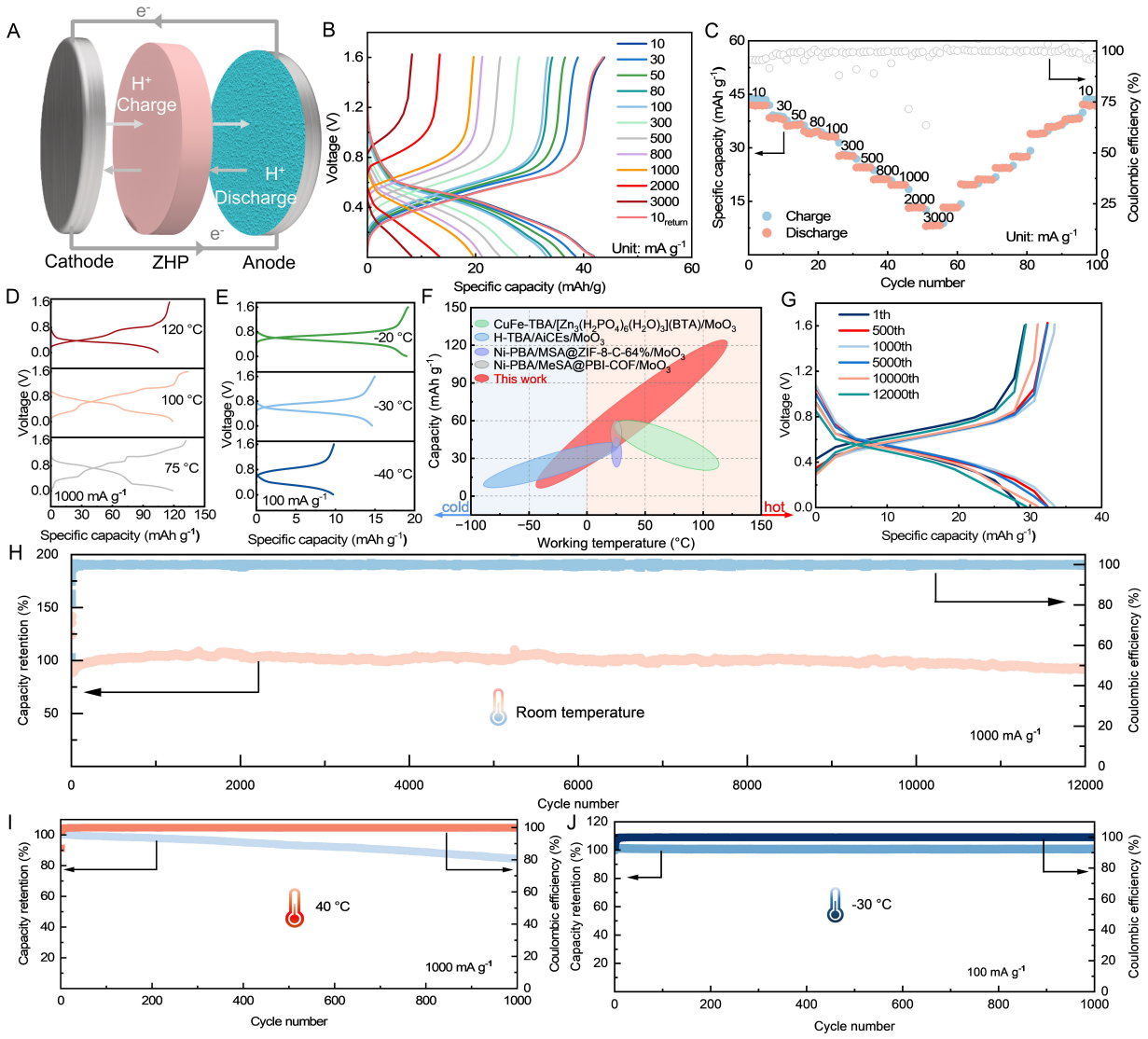

Figure 4. Electrochemical performance of H-TBA/ZHP/MoO_3 all-solid-state proton battery. (A) Device schematic; (B) GCD curves at different current densities; (C) Rate performance; (D and E) GCD profiles for full battery at various temperatures; (F) Comparison with reported systems; (G) Cycling GCD profiles at 1,000 mA·g^{-1}; (H-J) Cyclability and coulombic efficiency of the battery at 1,000 mA·g^{-1} at room temperature (H), at 1,000 mA·g^{-1} at 40 °C (I), and at 100 mA·g^{-1} at -30 °C (J). H-TBA: Pre-protonated Turnbull's blue analogue; ZHP: zirconium hydrogen phosphate; GCD: galvanostatic charge/discharge; PBA: Prussian blue analogue; MSA: methanesulfonic acid; ZIF: zeolitic imidazolate framework; MeSA: methylsulfonic acid; PBI: polybenzimidazole; COF: covalent organic framework.

Notably, upon returning to 10 mA·g^{-1}, the capacity is fully restored, indicating highly reversible electrochemical behavior and efficient proton transport within the ZHP electrolyte. In addition, the stable GCD profiles at different current densities further indicate rapid proton transfer within ZHP and no noticeable side reactions during cycling.

To validate the feasibility of ZHP in challenging conditions, the GCD test of the all-solid-state battery was carried out over 160 °C temperature range, as shown in Figure 4D and E and Supplementary Figure 15. At 120 °C and 1,000 mA·g^{-1}, the battery delivered a capacity of 116 mAh·g^{-1}, comparable to some aqueous batteries. Remarkably, even at -40 °C, the cell maintained a reversible capacity of 10 mAh·g^{-1} at 100 mA·g^{-1}, demonstrating exceptional wide temperature operability. Significantly, as shown in Figure 4F, the operating temperature range of this proton battery surpasses that of solid-state proton batteries utilizing AiCEs[36], $[Zn_3(H_2PO_4)_6(H_2O)_3](BTA)$[48], MSA@ZIF-8-C-X[33], and MeSA@PBI-COF[34]. Therefore, this proton battery

exhibits wider operating temperature range among reported all-solid-state proton batteries. As shown in Figure 4G, the GCD profiles at different cycles at room temperature nearly overlap, indicating that the proton intercalation and deintercalation reactions are highly reversible. The distinct anodic peak at 0.44 V and cathodic peak at 0.58 and 0.45 V in the cyclic voltammetry (CV) curves [Supplementary Figure 16] correspond to H^+ extraction and insertion, respectively, which is consistent with the GCD curve results. As shown in Figure 4H, the H-TBA/ZHP/MoO_3 cell delivers outstanding cycling durability at 1,000 mA·g^{-1} after activation at 10 mA·g^{-1}, retaining 92% capacity with a coulombic efficiency of 99.56% over 12,000 cycles. This cyclic performance is significantly superior to that of some reported all-solid-state proton batteries [Supplementary Figure 17, Supplementary Tables 5 and 6]. The H^+ transport kinetics before and after cycling were further evaluated. After cycling at 1,000 mA·g^{-1}, the full cell showed almost no obvious increase in interfacial resistance [Supplementary Figures 18-20], indicating the electrode and electrolyte interface was very stable. Moreover, the crystal structure and chemical bonds of ZHP before and after cycling were analysed by XRD and FTIR, respectively, as shown in Supplementary Figure 21. The XRD patterns showed almost no change before and after cycling, indicating that the rapid transport of H^+ did not cause structural damage to ZHP and further verifying the high compatibility between ZHP and electrodes. In addition, long-term cycling tests of the full battery were conducted at 40, -20, and -30 °C, as shown in Figure 4I and J, and Supplementary Figure 22. After 1,000 cycles at -20 and -30 °C, the capacity retention was almost 100%. At 40 °C, the cell retained 84.5% of its capacity. Such high electrochemical performance is encouraging, especially given that this is our initial trial conducted without the optimization of electrodes. The good long-term cycling performance over a wide temperature range and rapid H^+ transport are attributed to the ZHP's high structural stability and abundance of hydrogen bond networks.

In situ optical microscopy was used to assess the corrosiveness of ZHP toward electrodes and current collectors. As shown in Figure 5A and B, and Supplementary Video 1, vigorous bubble formation was observed at the electrolyte/current collector interface in the aqueous proton electrolyte (1 M H_3PO_4). Particularly, a severe gas evolution occurred on the Al foil current collector side, indicating that the aqueous proton electrolyte has a serious corrosiveness problem to current collectors. In contrast, when ZHP was used as the electrolyte, no gas bubbles were visually observed on the Al foil, cathode, and anode surfaces even after 12 h of contact, shown in Figure 5C-F, and Supplementary Videos 2 and 3. Moreover, the SEM and its corresponding elemental mapping were used to further characterize corrosiveness of the ZHP, as shown in Supplementary Figure 23. Almost no Al, Ti, Cu, Mo and Fe signals were detected in the ZHP electrolyte, indicating negligible corrosiveness toward the collectors (Al foil and Ti foil) and electrodes. ICP-OES analysis was conducted to assess corrosion-induced dissolution of current collectors and electrodes by detecting Al, Ti, Cu, Mo, and Fe in the electrolytes. For this analysis, the current collectors and electrodes were assembled into coin cell H-TBA/1 M H_3PO_4/MoO_3, Al/ZHP/Al and H-TBA/ZHP/MoO_3, respectively. The H-TBA/1 M H_3PO_4/MoO_3 battery, assembled with 1 M H_3PO_4 as the electrolyte, was analysed by ICP-OES after 1,000 GCD cycles. The result showed that Cu, Mo and Fe elements were detected in the liquid electrolyte [Supplementary Table 7], corresponding to dissolution ratios of 5.7% for Cu, 33.01% for Mo and 0.57% for Fe. In addition, the coin cell Al/ZHP/Al was kept for ten days, and the H-TBA/ZHP/MoO_3 cell was cycled for 12,000 GCD cycles before ICP-OES analysis. The results are consistent with EDS elemental mapping results, showing that the contents of Al, Ti, Cu, Mo and Fe in ZHP are almost negligible. Meanwhile, as shown in Supplementary Figures 24 and 25, SEM and its corresponding elemental mapping were performed on the positive and negative electrode materials after long-term cycling. The results show no element crossover problem between the electrode materials when ZHP was used as the electrolyte. According to these outcomes, ZHP can suppress gas evolution and corrosion, thereby improving the cycling stability of proton batteries. As shown in Supplementary Figure 26, since ZHP exhibits nearly no corrosive effect on Al foils, it is feasible to replace the Ti current collectors with more affordable Al current collectors, thus effectively reducing the production cost of proton batteries.

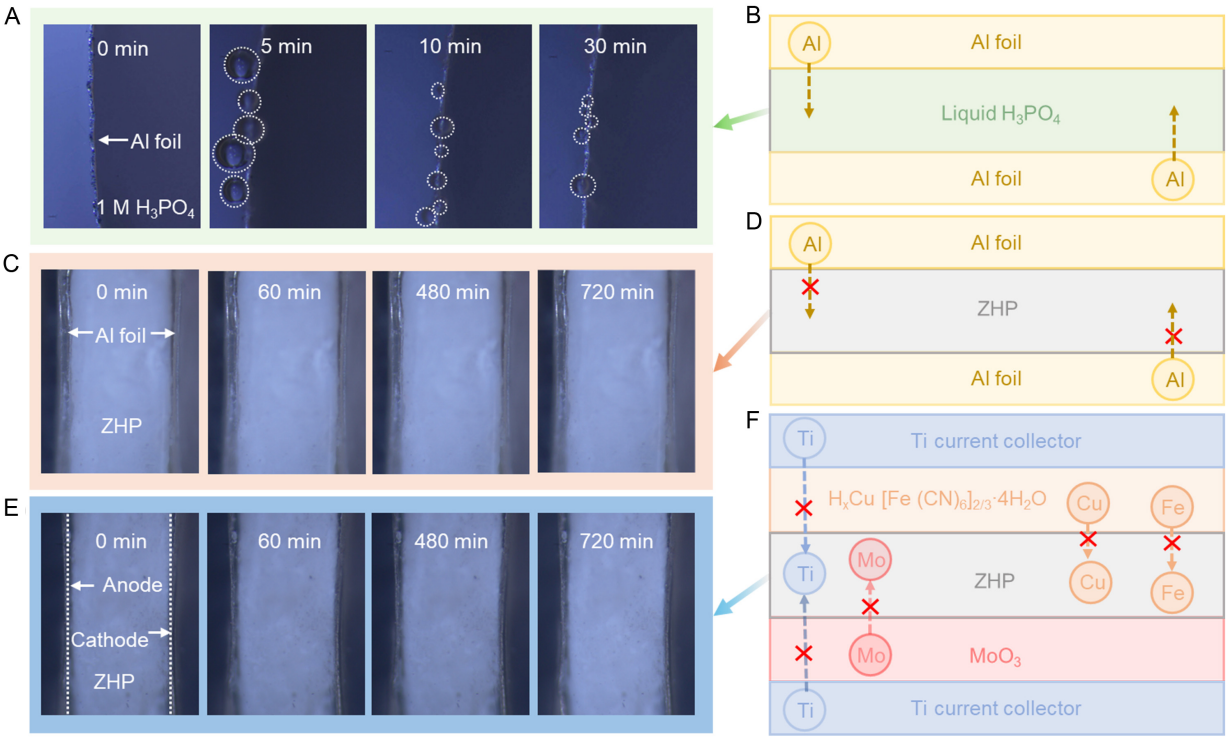

Figure 5. Corrosion behavior of ZHP electrolyte. (A, C and E) *In situ* optical images of 1 M H_3PO_4 and ZHP; (B, D and F) Schematic comparison between liquid H_3PO_4 and ZHP. ZHP: Zirconium hydrogen phosphate.

CONCLUSIONS

In summary, we have demonstrated that all-solid-state proton batteries can operate over a wide temperature range. The ZHP shows ultrafast proton transport from -40 to 120 °C (0.15-66.76 mS·cm^{-1}), a wide electrochemical stability window (~5.5 V), excellent stability, low corrosiveness toward current collectors and electrodes, and nonflammability. Those properties effectively address three major challenges in proton batteries including gas evolution, poor cycling stability, and limited operation under extreme temperatures. As a result, the all-solid-state proton battery exhibited stable cycling stability, retaining 92% of its initial capacity after 12,000 cycles at a current density of 1,000 mA·g^{-1} at room temperature. Additionally, it demonstrated stable cycling for 1,000 cycles, with capacity retention of 100% at -30 °C and 84.5% at 40 °C. Moreover, low corrosiveness of ZHP helps address the corrosion of electrode materials and current collectors caused by aqueous proton electrolyte, suggesting the possibility of using low-cost Al foils as current collectors. Although future improvements in cell capacity and further verification of proton transport behavior through appropriate collaborations are still needed, the present work opens a new avenue for the development of safe, durable, and wide-temperature proton batteries for practical energy-storage applications.

DECLARATIONS

Authors' contributions

Conducted the majority of the experiments, performed data analysis, and wrote the manuscript: Long, L.
Assisted with experiments and characterization analysis: Huang, Y.; Zheng, Y.
Assisted with experimental work and data interpretation: Guo, Y.; Liu, Y.
Performed device testing and characterization: Shen, Y.
Assisted with calculations and theoretical analysis: Jia, P.; Xu, Z.
Contributed to experimental design and manuscript revision: Dong, S.
Supervision, project administration, and funding acquisition: Shao, H.
All authors have read and agreed to the published version of the manuscript.

Availability of data and materials

Some results of supporting the study are presented in the Supplementary Materials. Other raw data that support the findings of this study are available from the corresponding authors upon reasonable request.

AI and AI-assisted tools statement

Not applicable.

Financial support and sponsorship

Shao, H. acknowledges the Shenzhen-Hong Kong-Macau Science and Technology Plan Project (Category C) (Grant No. SGDX20220530111004028), the Macau Science and Technology Development Fund (FDCT) for funding (FDCT No. 0013/2024/RIB1, FDCT-MOST joint project No. 0026/2022/AMJ and No. 006/2022/ALC of the Macao Centre for Research and Development in Advanced Materials [2022-2024]), the Multi-Year Research Grant (MYRG) from University of Macau (Project No. MYRG-GRG2024-00206-IAPME), Natural Science Foundation of Guangdong Province (Grant No. 2023A1515010765), Science and Technology Program of Guangdong Province of China (Grant No. 2023A0505030001), University of Macau Advanced Research Institute in Hengqin. Dong, S. acknowledges the National Natural Science Foundation of China (No. 52572234), and the Open Project of Jiangsu Key Laboratory of New Energy Devices & Interface Science (No. KFKT2025012).

Conflicts of interest

All authors declared that there are no conflicts of interest.

Ethical approval and consent to participate

Not applicable.

Consent for publication

Not applicable.

Supplementary Materials

Supplementary Materials

REFERENCES

1. Armand, M.; Tarascon, J. Building better batteries. *Nature* **2008**, *451*, 652-7. DOI PubMed
2. Xu, Y.; Wu, X.; Ji, X. The renaissance of proton batteries. *Small. Struct.* **2021**, *2*, 2000113. DOI
3. Yang, J. L.; Cao, J. M.; Zhao, X. X.; et al. Advanced aqueous proton batteries: working mechanism, key materials, challenges and prospects. *EnergyChem* **2022**, *4*, 100092. DOI
4. Huang, C.; Zhang, W.; Zheng, W. Proton batteries shape the next energy storage. *Energy. Storage. Mater.* **2023**, *61*, 102913. DOI
5. Su, Z.; Guo, H.; Zhao, C. Rational design of electrode-electrolyte interphase and electrolytes for rechargeable proton batteries. *Nano-Micro. Lett.* **2023**, *15*, 96. DOI PubMed PMC
6. Wu, S.; Guo, H.; Zhao, C. Challenges and opportunities for proton batteries: from electrodes, electrolytes to full-cell applications. *Adv. Funct. Mater.* **2024**, *34*, 2405401. DOI
7. Su, Z.; Ren, W.; Guo, H.; Peng, X.; Chen, X.; Zhao, C. Ultrahigh areal capacity hydrogen-ion batteries with MoO_3 loading over 90 mg cm^{-2}. *Adv. Funct. Mater.* **2020**, *30*, 2005477. DOI
8. Fleischmann, S.; Sun, Y.; Osti, N. C.; et al. Interlayer separation in hydrogen titanates enables electrochemical proton intercalation. *J. Mater. Chem. A.* **2020**, *8*, 412-21. DOI
9. Jiang, H.; Shin, W.; Ma, L.; et al. A high-rate aqueous proton battery delivering power below -78 °C via an unfrozen phosphoric acid. *Adv. Energy. Mater.* **2020**, *10*, 2000968. DOI
10. Dong, S.; Ren, H.; Yang, J.; et al. An aqueous proton battery under alkaline electrolyte. *Energy. Storage. Mater.* **2025**, *74*, 103888. DOI
11. Sui, Y.; Ji, X. Anticatalytic strategies to suppress water electrolysis in aqueous batteries. *Chem. Rev.* **2021**, *121*, 6654-95. DOI PubMed

12. Su, Z.; Chen, J.; Ren, W.; et al. "Water-in-sugar" electrolytes enable ultrafast and stable electrochemical naked proton storage. *Small* **2021**, *17*, 2102375. DOI PubMed
13. Shen, Y.; Liu, B.; Liu, X.; et al. Water-in-salt electrolyte for safe and high-energy aqueous battery. *Energy. Storage. Mater.* **2021**, *34*, 461-74. DOI
14. Xiao, D.; Zhang, L.; Li, Z.; Dou, H.; Zhang, X. Design strategies and research progress for Water-in-Salt electrolytes. *Energy. Storage. Mater.* **2022**, *44*, 10-28. DOI
15. Xu, Y.; Wu, X.; Jiang, H.; et al. A non-aqueous H_3PO_4 electrolyte enables stable cycling of proton electrodes. *Angew. Chem. Int. Ed.* **2020**, *59*, 22007-11. DOI PubMed
16. Vijayakumar, V.; Ghosh, M. Torris A. T., A.; et al. Water-in-Acid gel polymer electrolyte realized through a phosphoric acid-enriched polyelectrolyte matrix toward solid-state supercapacitors. *ACS. Sustain. Chem. Eng.* **2018**, *6*, 12630-40. DOI
17. Sahoo, R.; Mondal, S.; Pal, S. C.; Mukherjee, D.; Das, M. C. Covalent-organic frameworks (COFs) as proton conductors. *Adv. Energy. Mater.* **2021**, *11*, 2102300. DOI
18. Karlsson, C.; Strietzel, C.; Huang, H.; Sjödin, M.; Jannasch, P. Nonstoichiometric triazolium protic ionic liquids for all-organic batteries. *ACS. Appl. Energy. Mater.* **2018**, *1*, 6451-62. DOI
19. Wang, H.; Emanuelsson, R.; Karlsson, C.; Jannasch, P.; Strømme, M.; Sjödin, M. Rocking-chair proton batteries with conducting redox polymer active materials and protic ionic liquid electrolytes. *ACS. Appl. Mater. Interfaces.* **2021**, *13*, 19099-108. DOI PubMed PMC
20. Liao, M.; Ji, X.; Cao, Y.; et al. Solvent-free protic liquid enabling batteries operation at an ultra-wide temperature range. *Nat. Commun.* **2022**, *13*, 6064. DOI PubMed PMC
21. Peron, J.; Mani, A.; Zhao, X.; et al. Properties of Nafion® NR-211 membranes for PEMFCs. *J. Membr. Sci.* **2010**, *356*, 44-51. DOI
22. Li, H.; Liu, Y. Nafion-functionalized electrospun poly(vinylidene fluoride) (PVDF) nanofibers for high performance proton exchange membranes in fuel cells. *J. Mater. Chem. A.* **2014**, *2*, 3783-93. DOI
23. Jones, D. J.; Rozière, J. Recent advances in the functionalisation of polybenzimidazole and polyetherketone for fuel cell applications. *J. Membr. Sci.* **2001**, *185*, 41-58. DOI
24. Alberti, G.; Casciola, M. Layered metalIV phosphonates, a large class of inorgano-organic proton conductors. *Solid. State. Ionics.* **1997**, *97*, 177-86. DOI
25. Xie, Z.; Wu, H.; Wu, Q.; Ai, L. Synthesis and performance of solid proton conductor molybdovanadosilicic acid. *RSC. Adv.* **2018**, *8*, 13984-8. DOI PubMed PMC
26. Nimir, W.; Al-othman, A.; Tawalbeh, M. Unveiling zirconium phytate-heteropolyacids-ionic liquids membranes for PEM fuel cells applications up to 150 °C. *Int. J. Hydrogen. Energy.* **2025**, *107*, 3-14. DOI
27. Pili, S.; Argent, S. P.; Morris, C. G.; et al. Proton conduction in a phosphonate-based metal-organic framework mediated by intrinsic "free diffusion inside a sphere". *J. Am. Chem. Soc.* **2016**, *138*, 6352-5. DOI PubMed PMC
28. Chandra, S.; Kundu, T.; Kandambeth, S.; et al. Phosphoric acid loaded Azo (-N═N-) based covalent organic framework for proton conduction. *J. Am. Chem. Soc.* **2014**, *136*, 6570-3. DOI PubMed
29. Dane A. Boysenand, .; Haile, S. M.; Liu, H.; Secco, R. A. High-temperature behavior of CsH_2PO_4 under both ambient and high pressure conditions. *Chem. Mater.* **2003**, *15*, 727-36. DOI
30. Ponomareva, V.; Shutova, E. High-temperature behavior of CsH_2PO_4 and CsH_2PO_4-SiO_2 composites. *Solid. State. Ionics.* **2007**, *178*, 729-34. DOI
31. Haile, S. M.; Chisholm, C. R. I.; Sasaki, K.; Boysen, D. A.; Uda, T. Solid acid proton conductors: from laboratory curiosities to fuel cell electrolytes. *Faraday. Discuss.* **2007**, *134*, 17-39. DOI PubMed
32. Fop, S.; Vivani, R.; Masci, S.; Casciola, M.; Donnadio, A. Anhydrous superprotonic conductivity in the zirconium acid triphosphate $ZrH_5(PO_4)_3$. *Angew. Chem. Int. Ed.* **2023**, *62*, e202218421. DOI PubMed
33. Zhao, F. J.; Zhu, Y.; Chen, Y.; et al. Acidified nitrogen self-doped porous carbon with superprotonic conduction for applications in solid-state proton battery. *Small* **2023**, *20*, 2305765. DOI PubMed
34. Ren, X.; Song, J.; Zhang, G.; et al. Covalent-organic framework with superior proton conduction for solid-state proton battery application. *ACS. Mater. Lett.* **2024**, *6*, 4036-41. DOI
35. Li, H. Y.; Zhang, G. Q.; Luo, H. B.; et al. Zwitterionic engineering of vinylene-linked covalent organic frameworks for superior protonic electrolytes. *Angew. Chem. Int. Ed.* **2026**, *65*, e7677012. DOI PubMed
36. Wang, S.; Jiang, H.; Dong, Y.; et al. Acid-in-clay electrolyte for wide-temperature-range and long-cycle proton batteries. *Adv. Mater.* **2022**, *34*, 2202063. DOI PubMed
37. Meng, F.; Dong, X.; Wu, H.; Wu, Z.; Dou, H.; Zhang, X. Crystalline hydrogen enhanced dual-acid quasi-solid-state proton battery. *Adv. Funct. Mater.* **2025**, *35*, 2422079. DOI

38. Zhang, X.; Zhang, X.; Miao, Y.; et al. A rechargeable aqueous phenazine-Prussian blue proton battery with long cycle life. *J. Mater. Chem. A.* **2023**, *11*, 7152-8. DOI
39. Lei, Y.; Zhao, W.; Yin, J.; et al. Discovery of a three-proton insertion mechanism in α-molybdenum trioxide leading to enhanced charge storage capacity. *Nat. Commun.* **2023**, *14*, 5490. DOI PubMed PMC
40. Guo, H.; Wu, S.; Chen, W.; et al. Hydronium intercalation enables high rate in hexagonal molybdate single crystals. *Adv. Mater.* **2023**, *36*, 2307118. DOI PubMed
41. Hou, W.; Wang, E. Flow-injection amperometric detection of hydrazine by electrocalytic oxidation at a Prussian Blue film-modified electrode. *Anal. Chim. Acta.* **1992**, *257*, 275-80. DOI
42. Toby, B. H.; Von Dreele, R. B. *GSAS-II*: the genesis of a modern open-source all purpose crystallography software package. *J. Appl. Crystallogr.* **2013**, *46*, 544-9. DOI
43. Gilane, A.; Fop, S.; Sher, F.; Smith, R. I.; Mclaughlin, A. C. The relationship between oxide-ion conductivity and cation vacancy order in the hybrid hexagonal perovskite $Ba_3VWO_{8.5}$. *J. Mater. Chem. A.* **2020**, *8*, 16506-14. DOI
44. Chen, H.; Wong, L. L.; Adams, S. *SoftBV* - a software tool for screening the materials genome of inorganic fast ion conductors. *Acta. Crystallogr. B. Struct. Sci. Cryst. Eng. Mater.* **2019**, *75*, 18-33. DOI PubMed
45. Wong, L. L.; Phuah, K. C.; Dai, R.; Chen, H.; Chew, W. S.; Adams, S. Bond valence pathway analyzer - an automatic rapid screening tool for fast ion conductors within softBV. *Chem. Mater.* **2021**, *33*, 625-41. DOI
46. Krogh Andersen, A. M.; Norby, P.; Hanson, J. C.; Vogt, T. ChemInform abstract: preparation and characterization of a new 3-dimensional zirconium hydrogen phosphate, τ-$Zr(HPO_4)_2$. determination of the complete crystal structure combining synchrotron X-ray single-crystal diffraction and neutron powder diffraction. *ChemInform* **2010**, *29*, chin.199824003. DOI
47. Capitani, D.; Casciola, M.; Donnadio, A.; Vivani, R. High yield precipitation of crystalline α-zirconium phosphate from oxalic acid solutions. *Inorg. Chem.* **2010**, *49*, 9409-15. DOI PubMed
48. Ma, N.; Kosasang, S.; Yoshida, A.; Horike, S. Proton-conductive coordination polymer glass for solid-state anhydrous proton batteries. *Chem. Sci.* **2021**, *12*, 5818-24. DOI PubMed PMC
49. Hurd, J. A.; Vaidhyanathan, R.; Thangadurai, V.; Ratcliffe, C. I.; Moudrakovski, I. L.; Shimizu, G. K. H. Anhydrous proton conduction at 150 °C in a crystalline metal-organic framework. *Nature. Chem.* **2009**, *1*, 705-10. DOI PubMed
50. Horike, S.; Umeyama, D.; Inukai, M.; Itakura, T.; Kitagawa, S. Coordination-network-based ionic plastic crystal for anhydrous proton conductivity. *J. Am. Chem. Soc.* **2012**, *134*, 7612-5. DOI PubMed
51. Wang, L. S.; Patel, S. V.; Truong, E.; Hu, Y.; Haile, S. M. Phase behavior and superprotonic conductivity in the system $(1-x)CsH_2PO_4$ - xH_3PO_4: discovery of off-stoichiometric α-$[Cs_{1-x}H_x]H_2PO_4$. *Chem. Mater.* **2022**, *34*, 1809-20. DOI
52. Ohkoshi, S. I.; Nakagawa, K.; Tomono, K.; Imoto, K.; Tsunobuchi, Y.; Tokoro, H. High proton conductivity in prussian blue analogues and the interference effect by magnetic ordering. *J. Am. Chem. Soc.* **2010**, *132*, 6620-1. DOI PubMed
53. Vilčiauskas, L.; De Araujo, C. C.; Kreuer, K. Proton conductivity and diffusion in molten phosphinic acid (H_3PO_2): the last member of the phosphorus oxoacid proton conductor family. *Solid. State. Ionics.* **2012**, *212*, 6-9. DOI
54. Krueger, R. A.; Vilčiauskas, L.; Melchior, J.; Bester, G.; Kreuer, K. Mechanism of efficient proton conduction in diphosphoric acid elucidated via first-principles simulation and NMR. *J. Phys. Chem. B.* **2015**, *119*, 15866-75. DOI PubMed
55. Andersen, E. α-zirconium hydrogenphosphate, monohydrate. preparation, chemical properties and ac conductivity. *Solid. State. Ionics.* **1982**, *7*, 301-6. DOI
56. Yu, J.; Yu, H.; Yao, Z.; et al. A water-stable open-framework zirconium(iv) phosphate and its water-assisted high proton conductivity. *CrystEngComm* **2021**, *23*, 6093-7. DOI
57. Colodrero, R. M. P.; Olivera-pastor, P.; Cabeza, A.; Bazaga-garcía, M. Properties and applications of metal phosphates and pyrophosphates as proton conductors. *Materials* **2022**, *15*, 1292. DOI PubMed PMC